



**HAL**  
open science

# Silver-Bismuth Halide Double Salts for Lead-free Photovoltaics: Insights From Symmetry-Based Modeling

Bruno Cucco, Laurent Pedesseau, Claudine Katan, Jacky Even, Mikaël Kepenekian, George Volonakis

## ► To cite this version:

Bruno Cucco, Laurent Pedesseau, Claudine Katan, Jacky Even, Mikaël Kepenekian, et al.. Silver-Bismuth Halide Double Salts for Lead-free Photovoltaics: Insights From Symmetry-Based Modeling. Solar RRL, 2022, 6 (12), pp.2200718. 10.1002/solr.202200718 . hal-03829376

**HAL Id: hal-03829376**

**<https://hal.science/hal-03829376>**

Submitted on 15 May 2023

**HAL** is a multi-disciplinary open access archive for the deposit and dissemination of scientific research documents, whether they are published or not. The documents may come from teaching and research institutions in France or abroad, or from public or private research centers.

L'archive ouverte pluridisciplinaire **HAL**, est destinée au dépôt et à la diffusion de documents scientifiques de niveau recherche, publiés ou non, émanant des établissements d'enseignement et de recherche français ou étrangers, des laboratoires publics ou privés.

# Silver–Bismuth Halide Double Salts for Lead-Free Photovoltaics: Insights from Symmetry-Based Modeling

Bruno Cucco, Laurent Pedesseau, Claudine Katan, Jacky Even, Mikael Kepenekian,\* and George Volonakis\*

Ag/Bi halide double salts, also called rudorffites, constitute a promising path to achieve low-cost, high-efficiency lead-free optoelectronic devices, in particular solar cells. These materials present tunable gaps within the visible range, high short-circuit currents, and interesting efficiencies in outdoor and indoor devices. Herein, a combination of symmetry analysis and first-principles calculations is used to explore the structural, electronic, and optical properties of prototypical rudorffites solar cell absorbers  $\text{AgBiI}_4$  and  $\text{Ag}_3\text{BiI}_6$ . The challenges to model those ternary materials are first established. It is shown that Ag/Bi double salts cannot be modeled as random alloys. Second, a Wyckoff position splitting method is developed leading to the generation of model structures, which are unique for each compound, and agrees with experimental structural data. These structures are used to establish the optoelectronic properties of  $\text{AgBiI}_4$  and  $\text{Ag}_3\text{BiI}_6$ . Finally, the ideal photovoltaic performance of the materials is predicted through the spectral limited maximum efficiency approach. It is shown that  $\text{AgBiI}_4$  presents a slightly higher potential for solar cell applications, and the realized devices are mostly limited by the low open-circuit voltage. The structural models developed here can help unveiling complex properties of the materials and explore substitutional engineering within halide double salts.

## 1. Introduction


The last decade of photovoltaic research has been marked by impressive achievements when it comes to device efficiency and performance. In particular, in the field of emerging photovoltaics, lead halide perovskites, which exhibit remarkable optical and electronic properties, have conquered the place of most promising light absorbers for high-performance next-generation photovoltaic devices and as efficient building blocks for tandem solar cells. In fact, the latest tandem device has surpassed the 30% mark achieving a stunning certified power conversion efficiency (PCE) of 31.3%.<sup>[1]</sup> One common feature shared between high-performance materials is the presence of hazardous elements such as lead. Lead, in particular, has raised serious concerns regarding human health and environmental preservation.<sup>[2,3]</sup> The simplest substitution approach is to replace Pb with other atoms that share the same +2 oxidation state, thus allowing to maintain

charge neutrality and retaining the same crystalline structure. Unfortunately, perovskite materials and devices based on divalent metals from same column of the periodic table with Pb, such as Sn and Ge, were shown to be unstable when exposed to ambient conditions and are strongly affected by external variables such as illumination, temperature, moisture, and oxygen, due to the fast oxidation of  $\text{Sn}^{+2}$  and  $\text{Ge}^{+2}$  into  $\text{Sn}^{+4}$  and  $\text{Ge}^{+4}$ .<sup>[4–6]</sup> Another strategy is to replace two Pb with atoms in different oxidation states, significantly increasing the number of possible prototypical materials. Taking the standard  $\text{ABX}_3$  halide perovskite family for example (A is a monovalent cation, B a divalent metal, and X a halogen atom), one can combine monovalent and trivalent atoms at the B-site in a rock-salt like arrangement to form the so-called  $\text{A}_2\text{BB}'\text{X}_6$  halide double perovskites.<sup>[7–10]</sup> Among these, the materials that contain Ag and Bi, like  $\text{Cs}_2\text{BiAgBr}_6$ , have attracted significant interest for optoelectronic applications,<sup>[11–13]</sup> including solar cells.<sup>[14,15]</sup>

In 2017, Ag/Bi lead-free materials with the stoichiometric formula  $\text{Ag}_a\text{Bi}_b\text{I}_x$  ( $x = a + 3b$ ) were shown to be highly stable and were proposed as promising materials for solar cell applications, exhibiting well positioned optical bandgaps in the visible, between 1.4 and 2.0 eV.<sup>[16]</sup> These materials are in fact a mixture of the two salts:  $\text{AgI}$  and  $\text{BiI}_3$ , and Turkevych et al.<sup>[17]</sup> proposed to

B. Cucco, C. Katan, M. Kepenekian, G. Volonakis  
Univ Rennes  
INSA Rennes  
CNRS  
ISCR  
UMR 6226  
F-35000 Rennes, France  
E-mail: mikael.kepenekian@univ-rennes1.fr;  
yorgos.volonakis@univ-rennes1.fr

L. Pedesseau, J. Even  
Univ Rennes  
INSA Rennes  
CNRS  
Institut 695 FOTON  
UMR 6082  
F-35000 Rennes, France

 The ORCID identification number(s) for the author(s) of this article can be found under <https://doi.org/10.1002/solr.202200718>.

© 2022 The Authors. Solar RRL published by Wiley-VCH GmbH. This is an open access article under the terms of the Creative Commons Attribution-NonCommercial License, which permits use, distribution and reproduction in any medium, provided the original work is properly cited and is not used for commercial purposes.

DOI: 10.1002/solr.202200718

call these compounds “rudorffites”, after Walter Rüdorff and his pioneer work on  $\text{NaVO}_2$ , which forms a similar prototypical crystal lattice.<sup>[18]</sup> Members of this class of materials are easily processable and were successfully synthesized by spin coating techniques,<sup>[19]</sup> thermal coevaporation,<sup>[20]</sup> and through a solution atomization to produce aerosols.<sup>[21]</sup> Among these,  $\text{AgBiI}_4$  and  $\text{Ag}_3\text{BiI}_6$  have been shown to be particularly interesting candidates as demonstrated by their successful integration in solar cell devices, achieving remarkably high short-circuit current of  $10.7 \text{ mA cm}^{-2}$ ,<sup>[17,22]</sup> and PCE of up to 5.6%<sup>[23]</sup> for outdoor and 5.17%<sup>[22]</sup> for indoor devices. These PCE values are among the highest achieved for lead-free perovskites and perovskite-like materials, excluding the less stable Sn-based materials.<sup>[24]</sup> Materials that are more on the Bi-rich side like  $\text{AgBi}_2\text{I}_7$  tend to exhibit poorer performances in optoelectronic devices.<sup>[17,19]</sup> In a further attempt to improve device performance, the partial and total replacement of both Ag and Bi were investigated. Qu et al. showed that substituting Ag with Cu leads to the formation of  $\text{CuBiI}_4$ , and can improve the photoelectric performance of these materials, reaching photocurrents of  $500 \text{ mA W}^{-1}$ .<sup>[25]</sup> In the case of Bi substitutions, the phase diagram of Sb-doped  $\text{AgSb}_{1-x}\text{Bi}_x\text{I}_4$  materials and its thermochromism effects were also investigated by Gray et al.<sup>[26]</sup> Finally, the incorporation of Alkali metals, such as  $\text{Li}^+$ ,  $\text{Na}^+$ ,  $\text{K}^+$ ,  $\text{Rb}^+$ , and  $\text{Cs}^+$  by Wu et al., leads to efficiencies of up to 2.5% and a 6 month stability for  $\text{Ag}_3\text{BiI}_6$ -based photovoltaic devices.<sup>[27]</sup>

However, since employing these materials for solar cell applications there has been practically no thorough investigation of their electronic structure. Xiao et al.<sup>[28]</sup> first reported the band structure of  $\text{AgBiI}_4$ , employing a cubic  $\text{Fd}3\text{m}$  cell with ordered Ag and Bi atoms. In 2017, Sansom et al.<sup>[29]</sup> included the density of states for  $\text{AgBiI}_4$  using the lowest energy structure of Ag/Bi ordering in a supercell. The reason behind this lack of theoretical investigations is related to the absence of precise determination of the positions of Ag and Bi atoms from the available structural

data. Barone et al.<sup>[30]</sup> developed a high-throughput approach based on a machine learning algorithm to screen  $\text{AgBiI}_4$  structures and identify the most appropriate atomic arrangements. Employing an extensive number of possible structures key properties such as lattice parameters, simulated X-ray diffraction (XRD) patterns, density of states, bandgaps, and bulk moduli are obtained as an ensemble average of the screened structures.

In this work, we first thoroughly analyze the symmetry of the lattice of Ag/Bi double salts and show why these materials are particularly challenging to model. We show that the lattice symmetry and electronic properties strongly depend on the choice and ordering of the Ag/Bi positions. For two prototypical members of the family,  $\text{AgBiI}_4$  and  $\text{Ag}_3\text{BiI}_6$ , we develop an approach based on the splitting of the Wyckoff positions of the reported space groups to accurately describe the crystal lattices and the electronic properties. We directly compare our findings to the available experimental data, while we also employ modeling methods designed to treat random alloys (i.e., the special quasirandom structures [SQS] and the virtual crystal approximation [VCA]). We find that both structural and electronic correlations are better captured using subgroups generated by the Wyckoff position splitting approach. Having established the most reliable model, we move on to employ calculations from first principles and investigate in detail their electronic and optical properties. We use our findings to further probe the potential performance of these materials by means of their spectral limited maximum efficiency, and establish their actual photovoltaic potential.

## 2. Results and Discussion

### 2.1. Structure of Ag/Bi Double Salts

For  $\text{ABX}_3$  perovskites, heterovalent substitution of two  $\text{Pb}^{+2}$  with a monovalent  $\text{Ag}^+$  and a trivalent  $\text{Bi}^{+3}$  leads to the formation of

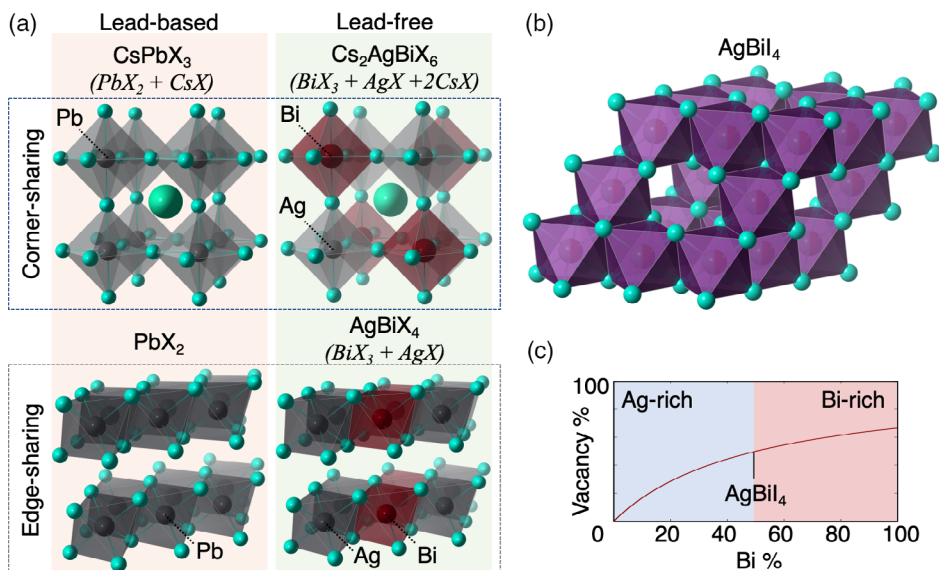


**Figure 1.** a) Schematic relationships between corner-sharing lead-based and lead-free Ag/Bi perovskites and the edge-sharing lead-based and Ag/Bi halide double salts ( $\text{PbX}_2$  corresponds to the 2H- $\text{PbX}_2$  polytype). b) Atomistic structure of  $\text{AgBiI}_4$  made of partially occupied Ag/Bi sites and vacancy sites. c) Vacancy percentage in the double salt structures as a function of the Bi-to-Ag ratio.

Ag/Bi double perovskites, like in the case of  $\text{Cs}_2\text{AgBiX}_6$ <sup>[7,31]</sup> (Figure 1a). In a similar way, substitution of two  $\text{Pb}^{+2}$  in the simple salt (e.g.,  $2\text{H-PbX}_2$ ) would lead to the formation of an  $\text{Ag}^+/\text{Bi}^{+3}$  double salt. This structure is shown in Figure 1a, where like the starting Pb salt, the double salts are made of a network of edge-sharing  $\text{AX}_6$  and  $\text{BX}_6$  octahedra. Yet, for the iodide material, i.e.,  $\text{AgBiI}_4$ , the actual lattice of the double salt differs to the simple  $2\text{H-PbX}_2$ , as the octahedra do not form ordered layers of octahedra separated by vacuum. Instead, the material arranges to form a 3D lattice that contains Ag, Bi, and vacancies sites ( $\Delta$ ), and is shown in Figure 1b. As these double salts are a mixture of Ag and Bi salts, there is a large phase space of materials that can be synthesized depending on the Ag-to-Bi ratio. This structural diversity is a direct consequence of the existence of vacant sites, as these allow to achieve charge neutrality when tuning the Ag-to-Bi ratio. This is not possible for the case of double perovskites, as there are no empty sites but a third salt (e.g.,  $\text{CsBr}$ ) that fixes the stoichiometry to  $\text{Cs}_2\text{AgBiX}_6$ .

Starting from the general class  $\text{Ag}_x\text{Bi}_y\Delta_z\text{I}_w$ , where  $x$ ,  $y$ ,  $z$ , and  $w$  denote the stoichiometry of each species, it is possible to derive the entire Ag–Bi–I family of materials based on two simple rules. First, the atomic species for these compounds are established by associating the right amount of halogens per metal site for a crystal lattice of edge-sharing octahedra. This leads to the equation:  $x + y + z = 2w$ . We can further normalize the halogens occupation at the anion sublattice and this expression is simplified to:  $x + y + z = 2$ . Next, the charge neutrality is defined based on the nominal oxidation states of each species, that is,  $\text{Bi}^{+3}$ ,  $\text{Ag}^{+1}$ ,  $\Delta^{+0}$ , and  $\text{I}^{-1}$ , leading to the equation:  $3y + x = 2$ . These two equations give the relation between Ag, Bi, and  $\Delta$ , and can be used to define the entire Ag–Bi–I materials phase space (Figure S1, Supporting Information), which was also shown by Turkevych et al.<sup>[17]</sup> Figure 1c presents the evolution of the vacancy ratio ( $\Delta\%$ ) per total metal sites in the unit cell, in relation to the Bi-to-Ag ratio ( $\text{Bi}\%$ ) in these compounds, which is given by the equation  $\Delta\% = 2\text{Bi}\% / (1 + 2\text{Bi}\%)$ . Here, it is shown that for compounds in Bi-rich limit, a larger number of vacant sites must exist in order to retain the charge neutrality of the system. For example, in the case of 0% Ag material:  $\text{BiX}_3$ , it contains 75% vacant sites, which is exactly the case of the  $\text{BiI}_3$  crystal.

Among the possible materials in the AgI– $\text{BiI}_3$  phase space, in 1985, Dzeranova et al. reported on the synthesis of  $\text{Ag}_3\text{BiI}_6$  and  $\text{AgBiI}_4$ , but were unable to assess their precise stoichiometry.<sup>[32]</sup> In 2013, Mashadieva et al. proposed that instead such system would consist of a combination of  $\text{Ag}_2\text{BiI}_5$  and  $\text{AgBi}_2\text{I}_7$ .<sup>[33]</sup> Yet, the atomic positions on the crystal structures were not determined. In 2016, Kim et al. investigated the  $\text{Ag}_2\text{BiI}_7$  describing it as a combination of  $\text{AgI}_6$  octahedra and  $\text{BiI}_8$  hexahedra, similar to the prototypical cubic  $\text{ThZr}_2\text{H}_7$ .<sup>[19]</sup> This structure was shown to be thermodynamically unstable by Xiao et al.,<sup>[28]</sup> and instead it was shown to adopt an Ag-deficient  $\text{Fd}\bar{3}\text{m}$  (227)  $\text{AgBiI}_4$  structure. The same kind of Ag-deficient structure was further reported and extensively investigated by Sansom et al., where they show that a perfect untwinned plate-like crystal of  $\text{AgBiI}_4$  can be associated to a rhombohedral  $\text{CdCl}_2$ -like cell with no ambiguity.<sup>[29]</sup> However, the same results show that for bulk powders, octahedral-faceted crystal, or polycrystalline films of  $\text{AgBiI}_4$ , it is not possible to unambiguously assign either a cubic defect spinel or a

rhombohedral  $\text{CdCl}_2$ -like structure. The challenge to assign a space group and identify the compound relates to the fact that the diffraction patterns are extremely similar, and can be resolved into different symmetry groups.<sup>[17,29]</sup> Moreover, the atomic positions can be determined using sites with partial occupations of the Wyckoff positions by different atomic species. The use of partial occupancies allows an accurate refinement of the crystalline structure, but poses a challenge for the atomistic modeling of the materials as one needs the exact atomic coordinates to place each atom (i.e., except within the VCA discussed below). Let us consider, for example, the experimental structure of  $\text{AgBiI}_4$  investigated and refined by H. C. Sansom<sup>[29]</sup> in the  $\text{Fd}\bar{3}\text{m}$  (227) space group. This material has Ag and Bi atoms sharing the 16c Wyckoff position with occupancy of 0.492 and 0.508, respectively. However, the I atoms are located at 32e sites. As a consequence, assigning coordinates for Ag and Bi would inevitably lead to a symmetry breaking of the experimental crystal lattice.

## 2.2. Random Alloys Models

In order to model materials that have partially occupied atomic sites, one of the most common approach is to employ supercells, where one can set up different atomic arrangements by assigning atom to different sites in the large cell. To assess the impact of ordering on the electronic structure, we perform density functional theory (DFT)-based calculations, using the PBE exchange–correlation functional, for a series of different orderings obtained first from the primitive and then the conventional unit cell of  $\text{AgBiI}_4$ . As shown in Figure S2, Supporting Information, within the primitive unit cell of  $\text{AgBiI}_4$  there are only two possible orderings, while within the conventional cell we identify five in-equivalent orderings. All the structures are fully optimized, with the computational details provided as Supporting Information. First, we compare the X-ray powder diffraction pattern for each modeled structure to the available experimental data. As shown in Figure 2a, different ordering representations lead to very different diffraction patterns, not matching the measured data. More importantly, we find large variations, of above 40%, for the electronic bandgap of the material depending on the atomic order between the cation species on the crystal lattice (Table S1, Supporting Information). Hence, the selected atomic order and the size of the employed supercell strongly affect both the diffraction pattern and the electronic structure of  $\text{AgBiI}_4$ .

Another approach would be to model these systems as random alloys, and employ for that purpose methods such as the SQS proposed by Zunger et al.<sup>[34]</sup> or the VCA by Bellaiche et al.<sup>[35]</sup> We employ both methods as the SQS method is developed to generate the structure that best mimics the figure's correlations of a perfectly random alloy, while the VCA introduces fictitious (virtual) atomic species that exhibit the averaged electronic configuration of the alloyed species in a single unit cell. To first assess the description of  $\text{AgBiI}_4$  structural properties, we compare the experimental XRD patterns and theoretical ones obtained within the SQS and VCA (Figure 2b). Both approaches improve the description with respect to the simple supercell models. In particular, the SQS presents an accurate compatibility between the experimental and theoretical XRD patterns, while the VCA leads to some shifts between experimental and

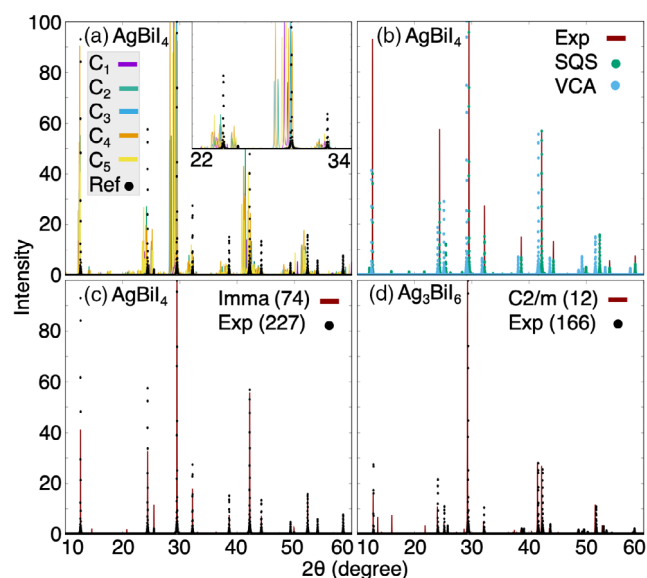


**Figure 2.** Simulated XRD patterns for different structural models and the experimental structure. a) Structures with different atomic orderings ( $C_i$ ) within a supercell of the  $Fd\bar{3}m$  (227)  $AgBi_4$  unit cell. The inset shows a zoom around the largest intensity peak. b)  $AgBi_4$  modeled as a random alloy within the SQS supercell and the VCA methods. c–d) Models of  $AgBi_4$  and  $Ag_3Bi_6$  in its subgroups by means of Wyckoff position splitting, respectively.

theoretical peaks. However, the electronic structures do not exhibit the same nice agreement, as within both the generated SQS cell and the VCA (Figure S3, Supporting Information),  $AgBi_4$  is predicted to be metallic, which is in direct contradiction to experiment.<sup>[29]</sup> Consequently,  $AgBi_4$  cannot be treated as a random alloy and a method to pick specific atomic coordinates

for Ag and Bi is needed. In fact, the experimentally proposed partial occupancies reflect the difficulty to unambiguously determine a space group and refine the specific Wyckoff positions of each Ag, Bi, and vacancies. This is consistent with the analysis of Sansom et al. for the untwinned plate-like crystal of  $AgBi_4$ , where each Ag and Bi is unambiguously associated with specific atomic positions.<sup>[29]</sup>

### 2.3. Symmetry-Based Model: Wyckoff Position Splitting

Starting from the available experimental data, we can model these systems and assign atomic positions by breaking the crystal symmetry in an elegant and controlled way. This is done by using the group/subgroup relations starting from the identified space group. Given, for example, a parent space group  $G$ , its symmetry operations can be reduced to another group  $H$  which is a subgroup of  $G$ . Hence, using the subgroup  $H$  the original Wyckoff positions can split to different sites with different multiplicities. The way the positions split happens is controlled by the group/subgroup transformations. This is known as Wyckoff position splitting and was investigated by  $H.$  Wondratschek.<sup>[36]</sup> Establishing this transformation is particularly important, as it allows using a different cell (e.g., a supercell) to describe the same structure, and maintains most symmetry operations of the original cell intact.

The Wyckoff position splitting for the case of  $AgBi_4$  is shown in Figure 3a. To validate the structural description, Figure 2c shows the comparison between the simulated XRD patterns of the experimental  $Fd\bar{3}m$  (227) structure and the material modeled within the subgroup  $Imma$  (74) after optimizing the atomic coordinates. As the XRD patterns agree well, we also look at the calculated average Bi–I (3.08 Å) and Ag–I (3.09 Å) bond lengths on the reduced symmetry structure. These are in good agreement

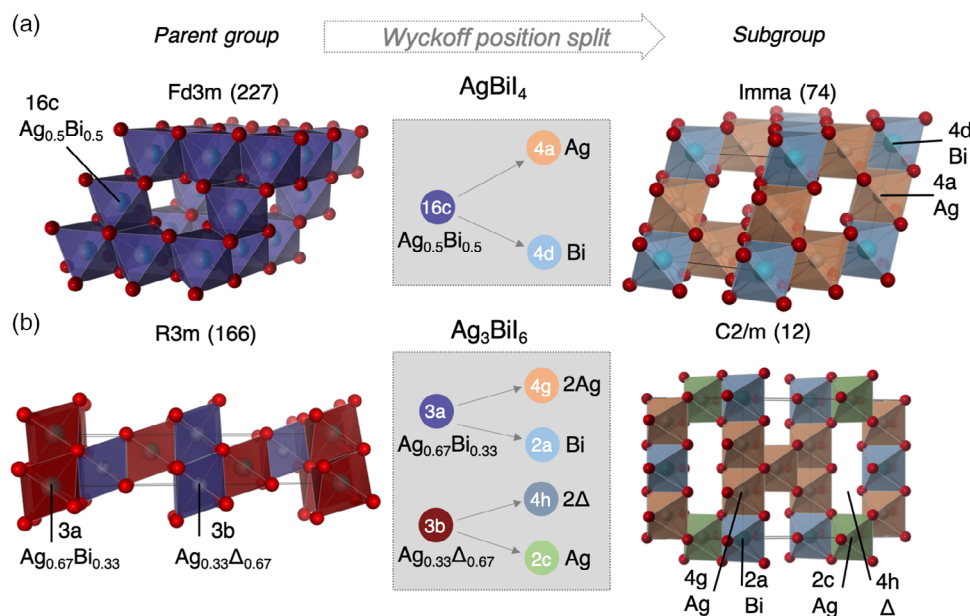


**Figure 3.** Predicted Wyckoff position splitting when a)  $AgBi_4$  is transformed from parent space group  $Fd\bar{3}m$  (227) to its subgroup  $Imma$  (74) and b)  $Ag_3Bi_6$  transformed from space group  $R\bar{3}m$  (166) to its subgroup  $C2/m$  (12). The octahedra color matches the Wyckoff sites of the parent and subgroup space groups as shown in the middle panel.

with the experimental structure (3.06 Å) measured by Sansom et al.,<sup>[29]</sup> and the structures based on the machine learning approach by Barone et al.,<sup>[30]</sup> which have Bi–I and Ag–I bond lengths of 3.14 and 3.09 Å, respectively. We employ this approach for the Ag-rich compound, Ag<sub>3</sub>BiI<sub>6</sub>. Oldag et al.<sup>[37]</sup> refined the lattice to the R3m (166) space group, with Ag and Bi atoms partially occupying the 3*a* Wyckoff site in ratios of 2/3 and 1/3, respectively. The site 3*b* is also partially occupied by 1/3 Ag and 2/3 vacancies, respectively. To split these two sites, we looked at the subgroups of the R3m group, and identified its subgroup C2/m (12), within which the 3*a* position splits to sites 2*a* and 4*g*, and the 3*b* position splits to the 2*c* and 4*h* sites, as shown in Figure 3b. By assigning respectively Ag and Bi to the 4*g* and 2*a* positions, the desired Ag/Bi ratio of the original structure is preserved. In a similar way, at the 3*b* position one can assign Ag and vacancies to the 2*c* and 4*h* sites, respectively. Such space group to subgroup transformation for Ag<sub>3</sub>BiI<sub>6</sub> also leads to a good agreement between the measured XRD pattern and the simulated one (Figure 2d). In fact, we also compare the radial distribution function calculated for the various models (Figure S4, Supporting Information), and we find important differences in the interatomic distances even for the atoms at short distances, which explain the strong effect of the model structures on the electronic properties. Consequently, these double salts crystallographic models selected using the Wyckoff splitting allow us to maintain most of the parent structure symmetries and move on to calculate the electronic and optical properties for this family of materials.

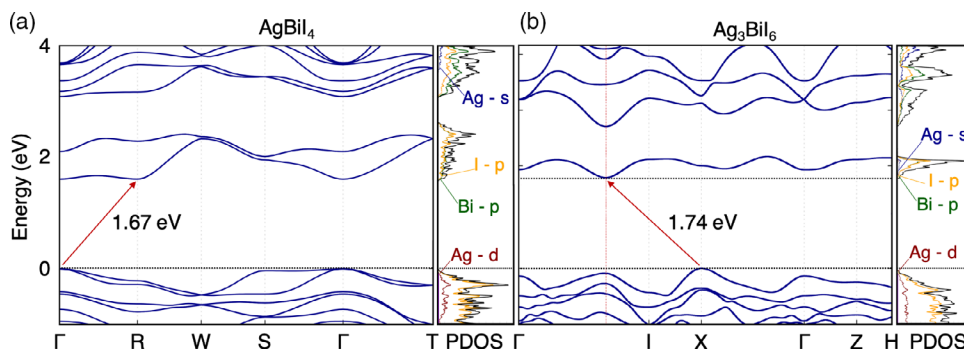
#### 2.4. Electronic Structure and Optical Properties

Figure 4 shows the electronic band structure and projected density of states (pDOS) for AgBiI<sub>4</sub> and Ag<sub>3</sub>BiI<sub>6</sub>. We choose to employ the DFT-PBE0 hybrid functional, which is known to overcome to a large extent the well-known bandgap underestimation of DFT (for all values, see Table S2, Supporting Information). AgBiI<sub>4</sub> has an indirect bandgap of 1.67 eV from  $\Gamma$  to R that is in close agreement with the experimental value of 1.73 eV.<sup>[29]</sup> We note that the conduction band minimum (CBM) is practically degenerate (less than 14 meV) between the  $\Gamma$  and the R-point. Ag<sub>3</sub>BiI<sub>6</sub> also has an indirect bandgap of 1.74 eV between the valence band maximum (VBM) located at X and the CBM that

is found at *k*-point (1/3, –1/3, 1/3), along the path between  $\Gamma$  and the I-point. The value of the bandgap is again in good agreement with the experimentally measured value of 1.83 eV.<sup>[38]</sup> The VBM of both materials is formed by hybridized I 5*p* and Ag 4*d* states, as seen in the pDOS for both materials. The CBM is made of hybridized Bi 6*p* and I 5*p* orbitals. We also note the bandwidth reduction of the conduction band when going from AgBiI<sub>4</sub> to Ag<sub>3</sub>BiI<sub>6</sub>. This is consistent with the reduction of the Bi/Ag ratio, as Bi is the main contributor to the CBM. Interestingly, the same electronic character is observed for corner-sharing Bi/Ag double perovskites,<sup>[31,39]</sup> i.e., a VBM dominated by I 5*p* orbitals and CBM resulting from a hybridization between Bi 6*p* and I 5*p* orbitals. These results suggest that even though the corner-sharing feature is lost, the electronic character is similar between these perovskite-like family of materials. The calculated bandgap (and band-edge compositions) of AgBiI<sub>4</sub> is in agreement with the work of Barone et al.<sup>[30]</sup> (i.e., 1.8 eV), and is well within the experimental range of 1.63–1.80 eV obtained by Sansom et al.<sup>[29]</sup>

To quantify the dispersion of the electronic bands, we calculate the effective masses at the band edges. For AgBiI<sub>4</sub>, we calculate a hole effective mass average of 0.77 *m<sub>e</sub>*, and for electrons we obtain an average mass of 0.42 *m<sub>e</sub>*. The detailed calculated effective masses are summarized in Table S3, Supporting Information, and we note a strong anisotropy in the reported mass tensor. Sansom et al. also report anisotropic electron and hole effective masses of AgBiI<sub>4</sub><sup>[29]</sup> in close agreement with our values. Their work further highlights the strong variation (more than 60%) of the masses for two different structural models (i.e., defect spinel and CdCl<sub>2</sub>). Such anisotropy can be attributed due to layers of Ag and Bi atoms, which are an artifact related to the cell type and size, hence here we choose to report the average mass as a more realistic quantity. For the Ag-rich compound Ag<sub>3</sub>BiI<sub>6</sub>, we obtain isotropic hole and electron effective masses of 0.57 *m<sub>e</sub>* and 0.55 *m<sub>e</sub>*, respectively. The isotropic masses are consistent with our symmetry-based model for which there are no arranged vacancy layers while using a prototypical layered-like model to describe Ag<sub>3</sub>BiI<sub>6</sub><sup>[38]</sup> results in fast and slow directions for charge carriers.

Next, we move on to investigate the optical properties of the two materials by means of calculating the band-to-band active transitions. Figure 5a shows a comparison between the



**Figure 4.** Interpolated hybrid DFT-PBE0 band structures for a) AgBiI<sub>4</sub> (Imma (74)) and b) Ag<sub>3</sub>BiI<sub>6</sub> (C2/m (12)). The conduction band bottom in (b) is located at the *k*-point (1/3, –1/3, 1/3) between the  $\Gamma$ –I path and it is represented in red dashed lines. The respective projected density of states are also shown.

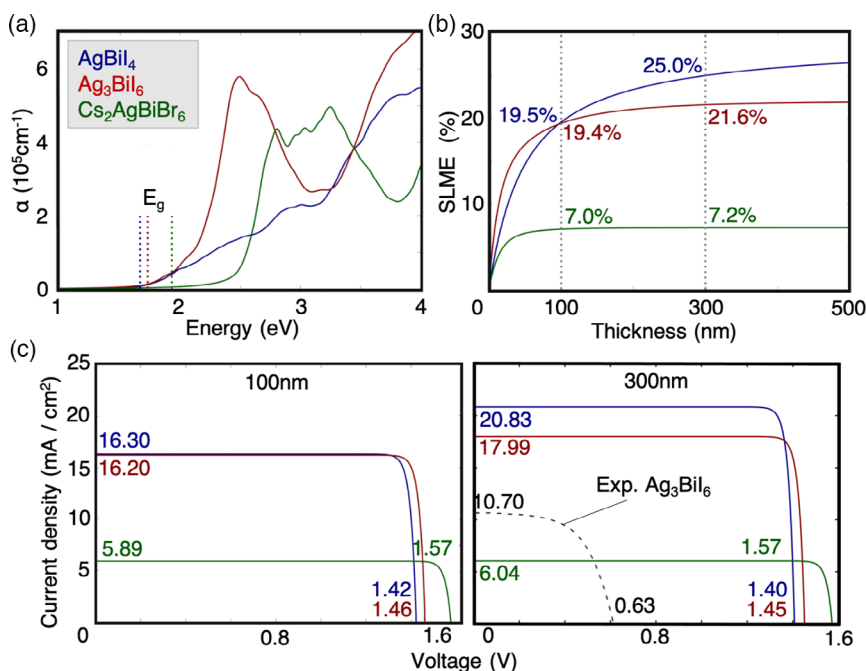


**Figure 5.** a) Absorption coefficient of  $\text{AgBiI}_4$  (Imma (74)),  $\text{Ag}_3\text{BiI}_6$  (C2/m (12)), and  $\text{Cs}_2\text{AgBiBr}_6$ ; dotted lines indicate the corresponding bandgaps  $E_g$ . b) SLME as a function of the thin-film thickness for  $\text{AgBiI}_4$  (Imma (74)),  $\text{Ag}_3\text{BiI}_6$  (C2/m (12)), and  $\text{Cs}_2\text{AgBiBr}_6$ . Current density as a function of voltage ( $J$ - $V$  plot) for a thickness of c) 100 nm and d) 300 nm. The black dashed curve represents the experimental curve obtained by Turkevich et al.<sup>[17]</sup> for a device containing  $\text{Ag}_3\text{BiI}_6$ .

calculated absorption coefficients for  $\text{AgBiI}_4$  and  $\text{Ag}_3\text{BiI}_6$ . The absorption onset for both materials are sharp close to the position of the calculated bandgaps ( $E_g$ ), as the first-allowed direct transition is found close in energy with  $E_g$ . For comparison with the Ag/Bi double salts, we also include the absorption coefficient, calculated at the same theory level, of the prototypical Ag/Bi double perovskite  $\text{Cs}_2\text{AgBiBr}_6$ .<sup>[40]</sup> The absorption onset is at higher energies, well above 2.3 eV, which is due to the large difference between the indirect bandgap (1.98 eV) and the first-allowed transition.  $\text{Ag}_3\text{BiI}_6$  shows stronger absorption in the range between 2 and 3 eV when compared to  $\text{AgBiI}_4$ , indicating a possible enhancement of the optical properties when more Ag is added. Interestingly, the same effect has been observed experimentally and reported by Turkevich et al.<sup>[17]</sup> when measuring optical absorption via UV-vis/NIR spectroscopy.

## 2.5. Theoretical Photovoltaic Performance

Having established the electronic and optical properties of these materials, we move to investigate the performance of these materials as solar cell absorber. The Shockley–Queisser (SQ) limit is one of the most used predictors when it comes to address the photovoltaic capabilities of a material.<sup>[41]</sup> Here, we employ the spectroscopic limited maximum efficiency (SLME) theory proposed by L. Yu and A. Zunger.<sup>[42]</sup> In comparison to the SQ limit, the SLME offers a refined description of the fraction of the radiative electron–hole recombination current  $f_r$  (For SQ  $f_r = 1$ ) taking into account its bandgap nature and absorption coefficient. All details on the formulation and

the computational implementation can be found in the Supporting Information.

Figure 5b shows the calculated SLME as a function of the thin-film thickness for  $\text{AgBiI}_4$ ,  $\text{Ag}_3\text{BiI}_6$ , and  $\text{Cs}_2\text{AgBiBr}_6$ . We observe that based on the calculated absorption coefficients, the Ag/Bi double salts are predicted to achieve superior SLME than the double perovskite, and that  $\text{AgBiI}_4$  can reach theoretical values of above 25%. Furthermore, one observes a steeper increase of the SLME with respect to the film thickness for the Ag-rich compound, with both materials reaching a plateau above 400 nm thickness. Interestingly, the  $\text{Ag}_3\text{BiI}_6$  outperforms  $\text{AgBiI}_4$  for thin-film thickness below 100 nm, which is consistent with a larger absorption coefficient. The higher SLME of  $\text{AgBiI}_4$  at higher thicknesses can be understood due to the smaller bandgap exhibited by  $\text{AgBiI}_4$ , which leads to a higher absorption of infrared photons that are not absorbed by  $\text{Ag}_3\text{BiI}_6$ . This contribution becomes more important as one increases the thin-film thickness, while the shape of the absorption coefficient becomes less important. This is given by  $a(E) = 1 - \exp(-2\alpha(E)L)$ , where  $a(E)$  is the absorptivity,  $\alpha(E)$  is the absorption coefficient, and  $L$  is the thin-film thickness.<sup>[42]</sup> As expected, SLME-predicted performances are higher than those for the devices made to-date. Turkevich et al.<sup>[17]</sup> report high performance for Ag-rich  $\text{Ag}_3\text{BiI}_6$ -based photovoltaic devices, yet based on the SLME we find that there is no intrinsic advantage with respect to  $\text{AgBiI}_4$ . Table S4, Supporting Information, contains a summary of the values obtained within SLME and SQ limit.

To further analyze the performance data, in Figure 5c we show the  $J$ - $V$  plot for two different thin-film thicknesses of 100 and 300 nm. We also note the correspondent open-circuit voltage

( $V_{oc}$ ) and short-circuit current ( $J_{sc}$ ). Comparing the two Ag/Bi double salts, the materials exhibit identical characteristics for the 100 nm thickness. The  $V_{oc}$  for both materials are very similar, which is related to their similar bandgaps. Going to 300 nm increases the estimated  $J_{sc}$  for both, yet slightly more for  $AgBiI_4$ , resulting at higher SLME values. With respect to the  $Cs_2AgBiBr_6$ , the Ag/Bi double salts exhibit slightly smaller  $V_{oc}$  due to their smaller bandgaps, but significantly higher values of  $J_{sc}$ . We note that photovoltaic devices based on  $Cs_2AgBiBr_6$  have experimentally reached a PCE of 3.11%,<sup>[14]</sup> which is above 40% of the ideal SLME, while  $Ag_3BiI_6$  devices achieved PCE of 5.6%, barely at 26% of the SLME. More generally, the maximum SLME values of  $AgBiI_4$  and  $Ag_3BiI_6$  are found slightly smaller than those of chalcopyrite-based materials like  $CuInS_2$  (29% efficiency<sup>[43]</sup>), and perovskite-based absorbers like  $MAPbI_3$  (31.5% efficiency<sup>[44]</sup>) and  $Ca_6Sn_4S_{10}O_4$  (32.53% efficiency<sup>[45]</sup>). Hence, there is room for experimental improvement of device performances. Comparing the experimental curves measured by Turkevich et al.,<sup>[17]</sup> shown in Figure 5c, the  $J_{sc}$  is at 60% of the ideal SLME value, while the  $V_{oc}$  is at 43%. Low  $V_{oc}$  can have several origins like, for example, the choice of unfitted electron or hole transport layers; thus, the SLME results indicate that a possible direction for improving power conversion efficiencies of Ag/Bi double salts devices is the optimization of the applied electron/hole transport layers and their interfaces.

### 3. Conclusions

We explored the structural details, electronic and optical properties, and ideal photovoltaic performances of two prototypes of the Ag/Bi halide double salts:  $AgBiI_4$  and  $Ag_3BiI_6$ . The particular challenges to describe their crystal lattice and atomic positions are identified, and we establish a theoretical approach that is based on experimental structures and symmetry, which enables the proper modeling, using a single cell, of their structure and description of their electronic properties. Our findings show that particular care should be taken, as the materials are not random alloys of the relevant halide salts. The structures generated by the symmetry-based approach developed here nicely reproduce the measured XRD patterns and predict that the materials are semiconductors with tunable bandgaps in the visible spectrum, in agreement with available experimental data and ML-based techniques. We report relatively low charge carrier effective masses, which favor the materials application in optoelectronic devices. The optical absorption spectrum showed that the Ag-rich material is more efficient at absorbing photons of energy below 2 eV. Yet, the calculated SLME clearly shows that  $AgBiI_4$  has the potential to achieve higher PCE values for film thicknesses above 100 nm. Both materials are predicted to perform better than Ag/Bi double perovskites as solar absorbers. Finally, as the developed structural models were shown to reliably describe the fundamental structural and optoelectronic properties of both  $AgBiI_4$  and  $Ag_3BiI_6$ , we believe that this work can be a valuable tool for exploring compounds within halide double salts, and enable higher theory level calculations to probe more complex properties such as the materials chemical and mechanical (photo-)stability.

### Supporting Information

Supporting Information is available from the Wiley Online Library or from the author.

### Acknowledgements

The research leading to these results has received funding from the Chaire de Recherche Rennes Metropole project, and from the European Union's Horizon 2020 program, through a FET Open research and innovation action under the grant agreement no. 862656 (DROP-IT). This work was granted access to the HPC resources of TGCC under the allocations 2020-A0100911434 and 2021-A0110907682 made by GENCI. The authors acknowledge PRACE for awarding us access to the ARCHER2, United Kingdom. The authors gratefully acknowledge discussions with O. Rubel on the calculation of the effective masses using the mstar code,<sup>[46]</sup> and I. Turkevych on the structural details of the Ag/Bi halide double salts.

### Conflict of Interest

The authors declare no conflict of interest.

### Data Availability Statement

The data that support the findings of this study are available in the supplementary material of this article.

### Keywords

electronic structures, halide double salts solar cells, lead-free photovoltaics, optical properties, spectral limited maximum efficiency, symmetry-based models

Received: August 5, 2022  
Revised: September 23, 2022  
Published online: October 26, 2022

- [1] Best research-cell efficiencies, <http://www.nrel.gov/>, **2022**.
- [2] M. Ren, X. Qian, Y. Chen, T. Wang, Y. Zhao, *J. Hazard. Mater.* **2022**, 426, 127848.
- [3] A. Babayigit, A. Ethirajan, M. Muller, B. Conings, *Nat. Mater.* **2016**, 15, 247.
- [4] N. K. Noel, S. D. Stranks, A. Abate, C. Wehrenfennig, S. Guarnera, A.-A. Haghighirad, A. Sadhanala, G. E. Eperon, S. K. Pathak, M. B. Johnston, A. Petrozza, L. M. Herz, H. J. Snaith, *Energy Environ. Sci.* **2014**, 7, 3061.
- [5] F. Hao, C. C. Stoumpos, D. H. Cao, R. P. H. Chang, M. G. Kanatzidis, *Nat. Photonics* **2014**, 8, 489.
- [6] A. W. Azhari, F. S. X. Then, D. S. C. Halin, S. Sepeai, N. A. Ludin, *IOP Conf. Ser.: Mater. Sci. Eng.* **2020**, 957, 012057.
- [7] E. T. McClure, M. R. Ball, W. Windl, P. M. Woodward, *Chem. Mater.* **2016**, 28, 1348.
- [8] M. R. Filip, S. Hillman, A. A. Haghighirad, H. J. Snaith, F. Giustino, *J. Phys. Chem. Lett.* **2016**, 7, 2579.
- [9] G. Volonakis, A. A. Haghighirad, R. L. Milot, W. H. Sio, M. R. Filip, B. Wenger, M. B. Johnston, L. M. Herz, H. J. Snaith, F. Giustino, *J. Phys. Chem. Lett.* **2017**, 8, 772.
- [10] G. Volonakis, A. A. Haghighirad, H. J. Snaith, F. Giustino, *J. Phys. Chem. Lett.* **2017**, 8, 3917.



- [11] B. Yang, J. Chen, S. Yang, F. Hong, L. Sun, P. Han, T. Pullerits, W. Deng, K. Han, *Angew. Chem. Int. Ed.* **2018**, *57*, 5359.
- [12] L. Zhou, Y.-F. Xu, B.-X. Chen, D.-B. Kuang, C.-Y. Su, *Small* **2018**, *14*, 1703762.
- [13] D. Wu, X. Zhao, Y. Huang, J. Lai, H. Li, J. Yang, C. Tian, P. He, Q. Huang, X. Tang, *Chem. Mater.* **2021**, *33*, 4971.
- [14] B. Wang, N. Li, L. Yang, C. Dall'Agnese, A. K. Jena, S.-I. Sasaki, T. Miyasaka, H. Tamiaki, X.-F. Wang, *J. Am. Chem. Soc.* **2021**, *143*, 2207.
- [15] X. Yang, Y. Chen, P. Liu, H. Xiang, W. Wang, R. Ran, W. Zhou, Z. Shao, *Adv. Funct. Mater.* **2020**, *30*, 2001557.
- [16] L. Wang, Y. Bao, S. Wang, F. Wang, C. Xie, K. T. Butler, X. Fan, *Cryst. Growth Des.* **2021**, *21*, 2850.
- [17] I. Turkevych, S. Kazaoui, E. Ito, T. Urano, K. Yamada, H. Tomiyasu, H. Yamagishi, M. Kondo, S. Aramaki, *ChemSusChem* **2017**, *10*, 3754.
- [18] W. Rüdorff, H. Becker, *Z. Naturforsch. B* **1954**, *9*, 614.
- [19] Y. Kim, Z. Yang, A. Jain, O. Voznyy, G.-H. Kim, M. Liu, L. N. Quan, F. P. García de Arquer, R. Comin, J. Z. Fan, E. H. Sargent, *Angew. Chem. Int. Ed.* **2016**, *55*, 9586.
- [20] M. Khazaei, K. Sardashti, C.-C. Chung, J.-P. Sun, H. Zhou, E. Bergmann, W. A. Dunlap-Shohl, Q. Han, I. G. Hill, J. Jones, D. C. Lupascu, D. B. Mitzi, *J. Mater. Chem. A* **2019**, *7*, 2095.
- [21] D. Danilović, D. K. Božanić, R. Dojčilović, N. Vukmirović, P. Sapkota, I. Vukašinović, V. Djoković, J. Bozek, C. Nicolas, S. Ptasinska, A. R. Milosavljević, *J. Phys. Chem. C* **2020**, *124*, 23930.
- [22] I. Turkevych, S. Kazaoui, N. Shirakawa, N. Fukuda, *Jpn. J. Appl. Phys.* **2021**, *60*, SCCE06.
- [23] N. Pai, J. Lu, T. R. Gengenbach, A. Seeber, A. S. R. Chesman, L. Jiang, D. C. Senevirathna, P. C. Andrews, U. Bach, Y.-B. Cheng, A. N. Simonov, *Adv. Energy Mater.* **2019**, *9*, 1803396.
- [24] P. Jiang, D. Acharya, G. Volonakis, M. Zacharias, M. Kepenekian, L. Pedesseau, C. Katan, J. Even, *APL Mater.* **2022**, *10*, 060902.
- [25] N. Qu, Y. Lei, X. Yang, X. Hu, W. Zhao, C. Zhao, Z. Zheng, *J. Mater. Chem. C* **2020**, *8*, 8451.
- [26] M. B. Gray, E. T. McClure, N. P. Holzappel, F. P. Evaristo, W. Windl, P. M. Woodward, *J. Solid State Chem.* **2021**, *297*, 121997.
- [27] M.-C. Wu, R.-Y. Kuo, Y.-H. Chang, S.-H. Chen, C.-M. Ho, W.-F. Su, *Oxford Open Mater. Sci.* **2021**, *1*, itab017.
- [28] Z. Xiao, W. Meng, D. B. Mitzi, Y. Yan, *J. Phys. Chem. Lett.* **2016**, *7*, 3903.
- [29] H. C. Sansom, G. F. S. Whitehead, M. S. Dyer, M. Zanella, T. D. Manning, M. J. Pitcher, T. J. Whittles, V. R. Dhanak, J. Alaria, J. B. Claridge, M. J. Rosseinsky, *Chem. Mater.* **2017**, *29*, 1538.
- [30] V. T. Barone, B. R. Tuttle, S. V. Khare, *J. Appl. Phys.* **2022**, *131*, 245701.
- [31] G. Volonakis, M. R. Filip, A. A. Haghighirad, N. Sakai, B. Wenger, H. J. Snaith, F. Giustino, *J. Phys. Chem. Lett.* **2016**, *7*, 1254.
- [32] K. B. Dzeranova, N. I. Kaloev, G. A. Bukhalova, *Russ. J. Inorg. Chem.* **1985**, *30*, 1700.
- [33] L. F. Mashadieva, Z. S. Aliev, A. V. Shevelkov, M. B. Babanly, *J. Alloys Compd.* **2013**, *551*, 512.
- [34] A. Zunger, S.-H. Wei, L. G. Ferreira, J. E. Bernard, *Phys. Rev. Lett.* **1990**, *65*, 353.
- [35] L. Bellaiche, D. Vanderbilt, *Phys. Rev. B* **2000**, *61*, 7877.
- [36] H. Wondratschek, *Miner. Petrol.* **1993**, *48*, 87.
- [37] T. Oldag, T. Aussieker, H.-L. Keller, C. Preitschaft, A. Pfitzner, *Z. Anorg. Allg. Chem.* **2005**, *631*, 677.
- [38] A. Crovetto, A. Hajjifarassar, O. Hansen, B. Seger, I. Chorkendorff, P. C. K. Vesborg, *Chem. Mater.* **2020**, *32*, 3385.
- [39] X. Li, B. Traoré, M. Kepenekian, L. Li, C. C. Stoumpos, P. Guo, J. Even, C. Katan, M. G. Kanatzidis, *Chem. Mater.* **2021**, *33*, 6206.
- [40] L. Schade, S. Mahesh, G. Volonakis, M. Zacharias, B. Wenger, F. Schmidt, S. V. Kesava, D. Prabhakaran, M. Abdi-Jalebi, M. Lenz, F. Giustino, G. Longo, P. G. Radaelli, H. J. Snaith, *ACS Energy Lett.* **2021**, *6*, 1073.
- [41] W. Shockley, H. J. Queisser, *J. Appl. Phys.* **1961**, *32*, 510.
- [42] L. Yu, A. Zunger, *Phys. Rev. Lett.* **2012**, *108*, 068701.
- [43] M. Bercx, N. Sarmadian, R. Saniz, B. Partoens, D. Lamoen, *Phys. Chem. Chem. Phys.* **2016**, *18*, 20542.
- [44] X. Ma, Z. Li, J. Yang, *J. Phys. Chem. C* **2021**, *125*, 10868.
- [45] J. Hu, C. Wang, Q. Li, R. Sa, P. Gao, *APL Mater.* **2020**, *8*, 111109.
- [46] O. Rubel, F. Tran, X. Rocquefelte, P. Blaha, *Comput. Phys. Commun.* **2021**, *261*, 107648.